Distinctive features of pretransitional behaviour between nematic phases as revealed by DDM

Nerea Sebastián, Luka Cmok, Andrej Petelin, Richard J. Mandle & Alenka Mertelj

Published online: 04 Mar 2024.

Submit your article to this journal

Article views: 114

View related articles

View Crossmark data

🔓 OPEN ACCESS | Check for updates

Distinctive features of pretransitional behaviour between nematic phases as revealed by DDM

Nerea Sebastián [ID][a], Luka Cmok[a], Andrej Petelin[a,b], Richard J. Mandle[c,d] and Alenka Mertelj [ID][a]

[a]Department of Complex Mater, Jožef Stefan Institute, Ljubljana, Slovenia; [b]Faculty of Mathematics and Physics, University of Ljubljana, Ljubljana, Slovenia; [c]School of Physics and Astronomy, University of Leeds, Leeds, UK; [d]School of Chemistry, University of Leeds, Leeds, UK

ABSTRACT

Pretransitional behaviour, with strong softening of the bend or splay elastic constants, is characteristic of two of the nematic to nematic phase transitions reported in the last decade. Such softening is strongly reflected in the pretransitional behaviour of the thermally excited director fluctuations. Here we give a comprehensive overview of the cross-Differential Dynamic Microscopy (c-DDM) method and its application to the investigation of thermal director fluctuations and phase transitions. For this, we build on the potentialities of the method for the investigation of the standard nematic phase of E7 to compare with the pretransitional behaviour of the nematic to twist bend nematic phase transition as well as the nematic to ferroelectric nematic transition.
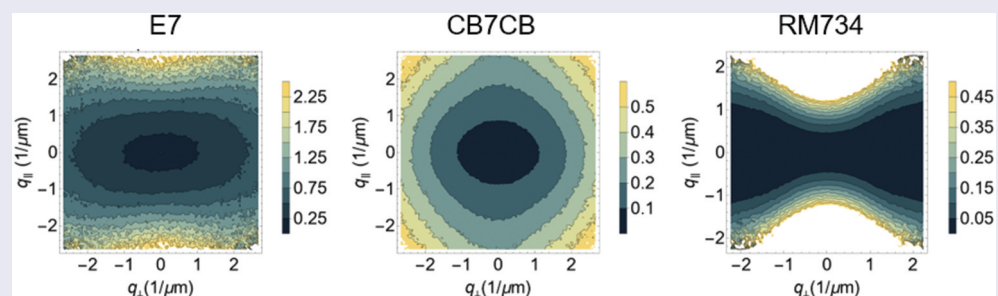
Introduction

The last decade has witnessed the discovery of two novel nematic (N) phases that have raised a lot of interest and expectations. The theoretically predicted [1] twist-bend nematic (N_{TB}) phase was identified as the low-temperature nematic phase in some systems of odd dimers [2–5]. In the N_{TB} phase, the nematic director twists and bends forming an oblique helicoid [6]. The helix can be either right- or left-handed, so the transition breaks the chiral symmetry of the normal N phase. The archetypal N_{TB} materials are the CBnCB family, consisting of two cyanobiphenyl mesogenic units linked through n methylene units. From $n = 5$ to $n = 13$ all the odd members of the family show a N-N_{TB} phase transition. Research on N_{TB} phases rapidly expanded through many materials, but notably the predominant phase sequence involves a weakly first-order N-N_{TB} phase transition [7] driven by the dramatic decrease towards

zero of the bend elastic constant K_3. In Dozov's precursor model [1], he showed that in the case of a system in which the bend elastic constant K_3 is small and goes to zero becoming negative for a critical temperature, the uniform N phase becomes unstable towards modulated phases, either a twist-bend or a splay-bend (N_{SB}) phase, being the balance between elastic constants the decisive factor. This model was followed by other theoretical approaches based on a macroscopic description of the nematic phase [8,9] with a notable contribution from L. Longa et al. [10–15].

More recently, the ferroelectric nematic (N_F) phase has been identified for a series of highly polar rod-shaped compounds [16]. In the N_F phase inversion symmetry is broken, leading to a 3D liquid with large spontaneous electric polarisation. The reference materials for N_F phases are RM734 [17,18] and DIO [19], both reported in 2017 to show several N phases. While the

first exhibits a direct N-N_F transition, the latter was reported to exhibit an intermediate phase (N-M2-N_F phase sequence). In the case of the direct N-N_F transition of RM734, it has been shown that the splay elastic constant K_1 is not only low in the N phase but strongly decreases when approaching the transition to the polar phase [20–22].

As with any new material, one of the first investigations relies on polarising optical microscopy investigations in thin confinements. For the trained eye, both phase transitions, both N-N_{TB} and N-N_F/N-M2 show evident pretransitional behaviour characterised by strong distinctive optical flickering for each case respectively. Such flickering is related to thermally excited director fluctuations. The rate and amplitude of such fluctuations depend on the viscoelastic properties of the material under consideration, and so for the N-N_{TB} transition, they are affected by the softening of bend fluctuations while for the N-N_F/N-M2 they are by the softening of the splay fluctuations.

Dynamic light scattering (DLS), in which the sample is illuminated by laser light and the scattered light is analysed as a function of the scattering vector and time, is a well-established technique for the study of viscoelastic properties of nematic liquid crystals [23], extensively discussed and applied in LC systems. Recently Cerbino and Trappe developed a method equivalent to DLS, differential dynamic microscopy (DDM), a near-technique based on optical microscopy based on digital Fourier microscopy [24]. DDM has been shown to be a very useful method for studies of the dynamical properties of soft matter. The method has been used to study, for example, diffusion motion of colloids [24–26], anisotropy of diffusion in colloids [27,28], non-diffusive motion of bacteria [29], kinetics of colloidal aggregation [30] and capillary waves [31]. Its advantage is that the measured part of the sample is imaged, so any unwanted processes, for example, diffusion of dust particles, can be easily identified.

Following the DDM method, the cross-Differential Dynamic Microscopy (c-DDM) method was reported by Arko and Petelin [32], based on two randomly triggered cameras imaging the same region of the sample, from which the cross-image differences and Fourier analysis based on the time delay between images are performed. This enhances the time resolution of the method well beyond the frame rate of a single camera and, therefore, gives access to faster dynamics (higher q vectors) than that accessible in standard DDM.

Such visual access to the area under examination is of great interest in the case of non-standard liquid crystals, e.g. ferroelectric nematic liquid crystals, which tend to form a hierarchy of domains under confinement. That is also certain for cases such as the N_{TB} phase. In the field of liquid crystals, DDM has been used to probe orientational dynamics in bulk nematic liquid crystals [33], critical fluctuations at magnetic field-induced structural transition in ferromagnetic liquid crystals [34], fluctuations during domain formation in ferromagnetic ferrofluid [35] and chiral fluctuations in unwound cholesterics [36]. In the case of N_F materials, it has been used to probe the π-twisted structure in antiparallel rubbed cells [37].

In this contribution, we aim to provide a comprehensive overview of the large potential of the DDM technique for the investigation of director fluctuations at the N-N_{TB} and N-N_F transitions, as exemplary for N-N transitions. For that, after the description of the theoretical background covering basic aspects of light scattering in nematic systems, DLS and DDM techniques, a comprehensive overview of the application of DDM for N phases is given covering selection rules and confinement effects among others. Such an overview serves as a reference for the interpretation of the investigations of pretransitional behaviour for the N-N_{TB} and N-N_F transitions reported next.

Theoretical background

Fluctuations in nematic liquid crystals

In nematic liquid crystals, the orientational fluctuations are the fundamental hydrodynamic excitations of the director field. In bulk, the eigenmodes of orientational fluctuations are over-damped plane waves, $\mathbf{e}_\beta \delta n_{0\beta}(e^{i\mathbf{q}\cdot\mathbf{r}} + c.c.)e^{-t/\tau_\beta}$. They have two dispersion branches, splay-bend ($\beta = 1$) and twist-bend ($\beta = 2$)(Figure 1), along the axes $\mathbf{e}_1$ and $\mathbf{e}_2$ of the coordinate system defined as

$$\mathbf{e}_3 \parallel \mathbf{n}_0, \mathbf{e}_2 = \frac{\mathbf{e}_3 \times \mathbf{q}}{|\mathbf{e}_3 \times \mathbf{q}|}, \mathbf{e}_1 = \mathbf{e}_2 \times \mathbf{e}_3 \qquad (1)$$

The relaxation rates are proportional to the ratio of the nematic elastic constants K_i and viscosity coefficients $\eta_\beta(\mathbf{q})$ [23],

$$\frac{1}{\tau_\beta}(\mathbf{q}) = \frac{K_\beta q_\perp^2 + K_3 q_\parallel^2}{\eta_\beta\left(\frac{q_\perp}{q_\parallel}\right)} \qquad (2)$$

where $q_\parallel$ and $q_\perp$ are the components of the wave vector parallel and perpendicular to the nematic director and $K_i(i = 1, 2, 3)$ denote splay, twist and bend elastic constants. The viscosity coefficients depend on the ratio $\frac{q_\perp}{q_\parallel}$ as
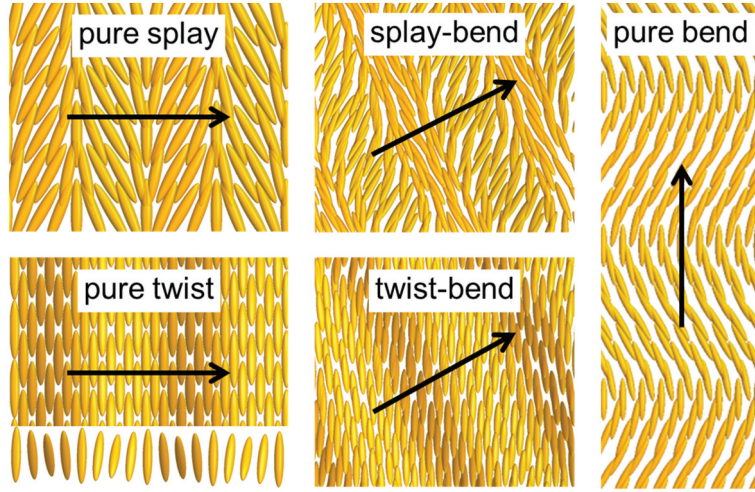
Figure 1. (Colour Online) Scheme of fluctuation eigenmodes in a nematic liquid crystal. Black arrows denote the wavevector **q**. In general, there are two branches - the splay-bend and twist-bend. When **q** is perpendicular to $\mathbf{n}_0$, they become pure splay and twist modes, and when **q** is parallel to $\mathbf{n}_0$, both modes become pure bend mode. The darker and lighter orange colours in twist cases denote the out of plane tilt of **n** with different signs, respectively.

$$\eta_1 = \gamma_1 - \frac{\left(\alpha_2 - \alpha_3 \left(\frac{q_\perp}{q_\parallel}\right)^2\right)^2}{\eta_c + (\alpha_1 + \alpha_3 + \alpha_4 + \alpha_5)\left(\frac{q_\perp}{q_\parallel}\right)^2 + \eta_b \left(\frac{q_\perp}{q_\parallel}\right)^4} \tag{3}$$

$$\eta_2 = \gamma_1 - \frac{\alpha_2^2}{\eta_c + \eta_a \left(\frac{q_\perp}{q_\parallel}\right)^2} \tag{4}$$

where γ_1 is the rotational viscosity, $\eta_{a,b,c}$ are Miesowicz viscosities and $\alpha_i (i = 1 - 5)$ are the Leslie viscosity parameters [23]. The **q**-dependent term in viscosities is due to the coupling between flow and nematic director, i.e. backflow, and reduces the viscosity coefficients of the fluctuation modes. It depends only on the ratio $\left(\frac{q_\perp}{q_\parallel}\right)$ and not on actual values of q. The pure twist viscosity $\left(\eta_2(q_\parallel = 0)\right)$ is not affected by the backflow and is equal to the rotational viscosity. Moreover, in calamitic nematic liquid crystals, the value of $|\alpha_3|$ is much smaller than γ_1 and η_c and, consequently, the pure splay viscosity, $\eta_1(q_\parallel = 0) = \gamma_1 - \alpha_3^2/\eta_b$, typically differs from γ_1 by a few percent.

When an eigenmode of the fluctuations is thermally excited, there is a deformation of the nematic director which causes an increase in the free elastic energy density,

$$f_{el} = \tfrac{1}{2}K_1(\nabla \cdot \mathbf{n})^2 + \tfrac{1}{2}K_2(\mathbf{n} \cdot (\nabla \times \mathbf{n}))^2 + \tfrac{1}{2}K_3(\mathbf{n} \times (\nabla \times \mathbf{n}))^2 \tag{5}$$

and, consequently, an elastic torque forces the director back in the equilibrium direction while a viscous torque opposes it. The expression for the relaxation rate

(Equation 2. 2) reflects this torque balance. The numerator comes from elastic torques deduced from the elastic free energy (Equation 5. 5), while the denominator originates in the viscous torques obtained from the linearised Leslie Ericksen equations [23].

The average square amplitudes of the fluctuation modes, $\langle \delta n_{0\beta}^2 \rangle$, can be calculated from Eq. 5 by using the equipartition theorem

$$\langle \delta n_{0\beta}^2 \rangle = \frac{k_B T}{V\left(K_\beta q_\perp^2 + K_3 q_\parallel^2\right)} \tag{6}$$

Here V is the volume of the sample, k_B Boltzmann constant and T temperature.

Effect of confinement
In an infinite sample, the spectrum of the fluctuations is continuous, i.e. all wave vectors are allowed, while in confined geometries it becomes discrete [38]. In a uniform nematic layer, the spectrum becomes discrete only in the direction perpendicular to the layer. For example, if backflow is not present, as is the case for the pure twist mode, the eigenmodes become sinusoidal standing waves with wave vectors that depend on the boundary conditions. For a layer spanning in z-direction from $-d/2$ to $d/2$, the pure twist mode becomes $\delta n_{0\beta}(e^{i\mathbf{q}_{2D} \cdot \mathbf{r}_{2D}} + c.c.) \cos(q_z z)e^{-t/\tau_\beta}$ with $\mathbf{q}_{2D}$ and $\mathbf{r}_{2D}$ being the wavevector and position in the xy plane, respectively. For strong boundary conditions, the allowed values of the wave vectors perpendicular to the layer are $q_{z,twist} = N\pi/d (N = 1, 2 \ldots)$, where d is the thickness of the layer.

In the bulk, due to the coupling between flow and nematic director, an eigenmode of the director orientational fluctuations is accompanied by a flow eigenmode, which is also a plane wave, which in the space coordinates is shifted for π/2 with respect to the corresponding director eigenmode, i.e. if a director fluctuation is described by $\cos(q_{m,z}z)$, flow is described by $\sin(q_{m,z}z)$. In a finite layer, such bulk solutions are not good solutions of nematodynamic equations, since they do not simultaneously satisfy the boundary conditions for the director $\delta n|_{boundary} = 0$ and flow $v|_{boundary} = 0$. This causes the dispersion relations of the eigenmodes to change in such a way that the crossings of the modes are avoided [39]. This will be discussed in more detail later.

Coupling to other (order) parameters

The nematic order parameter can be coupled to other physical quantities – also called secondary order parameters. In such cases, the number of director fluctuation modes increases. In the following, we will focus on systems in which the nematic order parameter is coupled to polarisation due to the flexoelectric effect. The fluctuation modes can be calculated from the free energy density,

$$f = f_{el} - \gamma_S \mathbf{n}(\ \cdot \mathbf{n}) \cdot \mathbf{P} - \gamma_B \mathbf{n} \times (\ \times \mathbf{n}) \cdot \mathbf{P} + \frac{1}{2} a \mathbf{P} \cdot \mathbf{P} + \frac{1}{2} b(\ \mathbf{P})^2 \quad (7)$$

Here, besides elastic free energy f_{el}, the second and third terms describe the coupling between the splay and bend deformations and electric polarisation respectively, where γ_S and γ_B are bare splay and bend flexoelectric coefficients. The last two terms are the lowest by symmetry allowed terms in $\mathbf{P}$ and $\partial P_i / \partial x_j$.

In the case of the phase transition from the nematic to the ferroelectric nematic phase, the pure splay fluctuations ($q_\parallel = 0$) are relevant. Here we will focus on this case. For that, we will assume that the polarization is parallel to the director, so $\mathbf{P} = P\mathbf{n}$. It is important to note here, that the free energy in Equation (7) . is written in the general form with $\mathbf{P}$ as a vector. Because $\mathbf{P}$ and $\mathbf{n}$ are parallel, only one vector is needed, which in our notation is $\mathbf{n}$ and it is mathematically a vector describing both, the nematic order parameter as $\mathbf{Q} = S(\mathbf{n} \otimes \mathbf{n} - \frac{1}{3}\mathbf{I})$ and polarization as $\mathbf{P} = P\mathbf{n}$. In such a notation, $\mathbf{Q}$ has inversion symmetry, while $\mathbf{P}$ does not. The symmetry of $\mathbf{Q}$ is already taken into account in the terms related to the nematic order parameter. Because we focus on the transition, only the lowest terms associated with $\mathbf{P}$ are included in Equation (7) because in the N phase $\langle \mathbf{P} \rangle = 0$. This description is only good very close to the phase transition.

We assume that the director is homogeneously aligned along the x-axis and, consequently, the average <p> is zero. The fluctuations can be described by a small angle φ between the fluctuating director $\mathbf{n}(x, t) = (\cos(\varphi(x, t)), 0, \sin(\varphi(x, t)))$ and the average director $\mathbf{n}_0$, and normalized $P_n = P/P_r$, where P_r is an arbitrary normalization constant. The renormalized coefficients are: $a_r = aP_r^2, \gamma_r = \gamma_S P_r$, and $b_r = bP_r$. The free energy density (Eq. 7) expanded to the second order in φ and P simplifies to

$$f_{fl} = \frac{1}{2}\left(a_r P_r^2 + b_r\left(\frac{\partial P_n}{\partial x}\right)^2 - 2\gamma_r P_n \frac{\partial \varphi}{\partial x} + K_1\left(\frac{\partial \varphi}{\partial x}\right)^2\right) \quad (8)$$

From which the linear coupled dynamic equations for φ and P_n follow

$$\eta_1 \frac{\partial \varphi}{\partial \tau} = K_1 \frac{\partial^2 \varphi}{\partial x^2} - \gamma_r \frac{\partial P_n}{\partial x} \quad (9)$$

$$\eta_{P_0} \frac{\partial P_n}{\partial \tau} = b_r \frac{\partial^2 P_n}{\partial x^2} - \gamma_r \frac{\partial \varphi}{\partial x} + a_r P_n \quad (10)$$

Here η_1 is the effective splay orientational viscosity and η_{P0} the dissipation coefficient for P. The two solutions of Eqs. 9 and 10 are: $\varphi_{1,2} = \pm\varphi_{01,02} \sin(qx)e^{-t/\tau_{01,02}}$ and $P_{1,2} = \pm P_{01,02} \cos(qx)e^{-t/\tau_{01,02}}$, with the relaxation rates

$$\frac{1}{\tau_{01,02}} = \frac{(b_r q^2 + a_r)\eta_1 + K_1 q^2 \eta_{P_0} \mp \sqrt{(b_r q^2 + a_r)^2 \eta_1^2 - 2q^2\left(b_r K_1 q^2 + K_1 a_r - 2\gamma_r^2\right)\eta_1 \eta_p + K_1^2 q^4 \eta_{P_0}^2}}{2\eta_1 \eta_{P_0}} \quad (11)$$

For small q they simplify to

$$\frac{1}{\tau_{01}} = \frac{K_1 - \frac{\gamma_s^2}{a}}{\eta_1} q^2 \quad (12)$$

$$\frac{1}{\tau_{02}} = \frac{a}{\eta_P} + \left(\frac{b}{\eta_P} + \frac{\gamma_s^2}{\eta_1 a}\right)q^2 \quad (13)$$

Here, $\eta_P = \eta_{P0} P_r^2$.

The first mode is of a hydrodynamic type and is mainly a director mode. If the splay elastic constant is replaced by an effective elastic constant

$$K_{1,eff} = K_1 - \frac{\gamma_s^2}{a} \quad (14)$$

the relaxation rate Eq.(12) becomes identical to the relaxation rate of the splay fluctuations [23] with the splay elastic constant replaced by the effective one. This shows that in a usual measurement of the splay elastic constant by either dynamic light scattering (DLS) or by Frederiks transition, always the effective elastic constant Eq. (14) is measured. The second mode is of an optic type with a relaxation rate which is finite at $q = 0$ and this is the collective mode observed in the dielectric spectroscopy.

The average square amplitudes of the fluctuation modes can be calculated by using the equipartition

theorem. For small q the amplitudes of the director fluctuations are given as

$$\langle \varphi_{01}^2 \rangle = \frac{k_B T}{V K_{1,eff} q^2} \qquad (15)$$

$$\langle \varphi_{02}^2 \rangle = \frac{2 k_B T \gamma^2 \eta_{P0}^2}{V a^3 \eta_1^2} q^2 \qquad (16)$$

Here V is the volume of the sample. The first mode is much slower and has a much larger amplitude, and is the one measured in DLS experiments. On the other hand, the average square amplitudes of the polarisation fluctuation modes at $q = 0$ are

$$\langle P_{01}^2 \rangle = \frac{2 k_B T \gamma^2}{V K_{1,eff} a^2} \qquad (17)$$

$$P_{02}^2 = \frac{2 k_B T}{V a} \qquad (18)$$

In dielectric experiments, the modes at $q = 0$ and with finite relaxation rates are measured, which in our case is the second mode. That is, the amplitude of the collective mode measured in the dielectric spectroscopy is proportional to $\langle P_{02}^2 \rangle$ [40]

$$\Delta \varepsilon_\parallel \propto \langle P_{02}^2 \rangle \propto \frac{1}{a} \qquad (19)$$

In the Landau description of the ferroelectric phase transition the coefficient in the quadratic term of $\mathbf{P}$ is the inverse of the electric susceptibility. (Eq. 17) and (Eq.18) show that in our case, the contribution of the dielectric susceptibility that drives the ferroelectric phase transition is the second mode and

$$a = \frac{1}{\varepsilon_0 \Delta \varepsilon_\parallel} \qquad (20)$$

where ε_0 is the vacuum permittivity.

Similarly, for the pure bend mode ($q_\perp = 0$) in which flexoelectric polarization is perpendicular to $\mathbf{n}$, and which is relevant for the transition to the N_{TB} phase, it can be shown that for small q, relaxation rates corresponding to pure bend are given by [41]

$$\frac{1}{\tau_{01}} = \frac{K_3 - \frac{\gamma_B^2}{a}}{\eta_3} q^2 \qquad (21)$$

$$\frac{1}{\tau_{02}} = \frac{a}{\eta_P} + \left(\frac{b}{\eta_P} + \frac{\gamma_B^2}{\eta_3 a} \right) q^2 \qquad (22)$$

While the transition from N to N_F phase can be well described by this model, the transition to the N_{TB} phase is dominated by higher-order terms in elastic energy [9,13].

Experimental

Light scattering on fluctuations

The director fluctuations give rise to fluctuations of the dielectric tensor which cause strong scattering of light, i.e. the turbidity of the nematic phase. In linear theory, the director field can be written as a sum of a static part, $\mathbf{n}_0$, that describes the equilibrium configuration, and a small, time-dependent part $\delta \mathbf{n}(\mathbf{r}, t)$ that describes thermal orientational fluctuations around the equilibrium configuration. In frustrated confined geometries and around defects the static part $\mathbf{n}_0$ depends on position; however, in this paper, we will discuss only the case of ordered nematic, where $\mathbf{n}_0$ is uniform (independent of $\mathbf{r}$). In such a case, for a given scattering vector $\mathbf{q}$, the scattered light amplitude depends on two independent Fourier components $\delta n_1(\mathbf{q})$ and $\delta n_2(\mathbf{q})$ of the Fourier transform of the director fluctuations, corresponding to the splay-bend and the twist-bend excitations as described in the previous section, respectively.

The optical dielectric tensor of a nematic liquid crystal can be written as

$$\underline{\varepsilon}(\mathbf{r}, t) = \varepsilon_\perp \underline{\mathbf{I}} + \varepsilon_a n(\mathbf{r}, t) \otimes \mathbf{n}(\mathbf{r}, t) \qquad (23)$$

where $\varepsilon_a = \varepsilon_e - \varepsilon_o$ with ε_e and ε_o the components of the optical dielectric tensor along (extraordinary) and perpendicular (ordinary) to the director. The fluctuations of the dielectric tensor are dominated by the orientational fluctuations of the nematic director, and their Fourier components can be written in the coordinate system defined above as functions of $\delta n_1(\mathbf{q})$ and $\delta n_2(\mathbf{q})$

$$\delta \underline{\tilde{\varepsilon}}(\mathbf{q}, t) \approx \varepsilon_a \begin{bmatrix} 0 & 0 & \delta n_1(\mathbf{q}) \\ 0 & 0 & \delta n_2(\mathbf{q}) \\ \delta n_1(\mathbf{q}) & \delta n_2(\mathbf{q}) & 0 \end{bmatrix} \qquad (24)$$

The best way to observe them is by dynamic light scattering (DLS). In DLS experiments, the intensity autocorrelation function is measured, which is connected to the electric field autocorrelation function of the scattered light, $G^1(\mathbf{q}_s, t) = \langle E_s(\mathbf{q}_s, t') E_s^*(\mathbf{q}_s, t' + t) \rangle$ [42]. For weak scattering $G^1(\mathbf{q}_s, t)$ is proportional to the dynamical structure function

$$B(\mathbf{i}, \mathbf{k}_i \rightarrow \mathbf{f}, \mathbf{k}_f, t) = k_0^4 \delta \tilde{\varepsilon}_{if}(\mathbf{q}_s, t') \delta \tilde{\varepsilon}_{if}^*(\mathbf{q}_s, t' + t) \qquad (25)$$

where $\mathbf{i}, \mathbf{f}, \mathbf{k}_i$ and, $\mathbf{k}_f$ are the polarisations and wave vectors of the incoming and scattered light and, $\mathbf{q}_s = \mathbf{k}_f - \mathbf{k}_i$. For $t = 0$, the electric field autocorrelation function is simply the intensity of the scattered light and Expression is the optical structure function. The measured component of the optical dielectric tensor is selected by the polarizations, $\delta \tilde{\varepsilon}_{if}(\mathbf{q}_s, t) = \mathbf{f} \cdot \delta \underline{\tilde{\varepsilon}}(\mathbf{q}_s, t) \cdot \mathbf{i}$. The dynamic structure function is a time correlation function of the Fourier

component of the optical dielectric tensor with a wavevector corresponding to the scattering vector. In the systems where the eigenmodes of the fluctuations are plane waves, a given Fourier component therefore corresponds to an eigenmode with the eigenvector equal to the scattering vector, $\mathbf{q} = \mathbf{q}_s$. Thus, in bulk nematic liquid crystals the direction of the scattering vector and the polarizations can be chosen so that either twist-bend or splay-bend mode is observed. In such a case, the electric field autocorrelation function obtained in the DLS experiment is an exponentially decaying function with a relaxation rate equal to the relaxation rate (Eq. 2) of the chosen eigenmode of the orientational fluctuations.

The intensity of the scattered light $I_{s,\beta}$ from a given mode depends on the projections of the polarisations on the eigenaxes (Eq. 1), determined by the so-called geometrical factor

$$S_\beta = (\boldsymbol{i} \cdot \mathbf{e}_3)(\boldsymbol{f} \cdot \mathbf{e}_\beta) + (\boldsymbol{i} \cdot \mathbf{e}_\beta)(\boldsymbol{f} \cdot \mathbf{e}_3) \qquad (26)$$

where $(\beta = 1, 2)$, on the square of the optical anisotropy ε_a and on the amplitudes of the nematic fluctuations

$$I_{s,\beta}(\mathbf{q}) \propto \frac{(\varepsilon_a)^2 S_\beta^2}{K_\beta q_\perp^2 + K_3 q_\parallel^2} \qquad (27)$$

In bulk liquid crystals, the dynamical structure function is then proportional to

$$B(\boldsymbol{i}, \mathbf{k}_i \rightarrow \boldsymbol{f}, \mathbf{k}_f, t) \propto \sum_\beta I_{s,\beta}(\mathbf{q}) e^{-t/\tau_\beta(\mathbf{q})} \qquad (28)$$

with $\mathbf{q} = \mathbf{k}_f - \mathbf{k}_i$.

Dynamic light scattering experiments

A standard setup for DLS experiments consists of a frequency-doubled diode-pumped Nd:YAG laser (532 nm, 80 mW), a single-mode optical fibre to collect the scattered light within one coherence area [43], a cross-correlation detector (e.g ALV APD), and a correlator (e.g. ELC-6010/160) to obtain the autocorrelation function of the scattered light intensity. Based on Eq. (26) it is important to choose the direction and the polarization of the incoming and detected light so that pure modes can be observed. Two
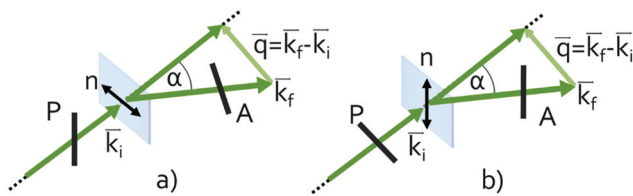
scenarios are particularly useful and are depicted in Figure 2. For a scattering geometry in which the director is in the scattering plane, and incoming and detected polarizations are selected orthogonal to the scattering plane and contained in it respectively (Figure 2(a)), it can be shown that $S_1^2 = 0$ at any angle and that for $\alpha = 35°$ almost pure bend mode $K_3 q_\parallel^2 / \eta_2$ can be detected. For the second depicted geometry, where the director is orthogonal to the scattering plane and incoming and detected polarizations correspond to the ordinary and extraordinary components respectively, $q_\parallel^2 = 0$ at any detection angle, and at low scattering angles ($\alpha = 2°$) pure twist mode $K_2 q_\parallel^2 / \eta_2$ is detected, while at larger angles ($\alpha = 35°$) is the pure splay mode $K_1 q_\parallel^2 / \eta_1$ the one experimentally accessible. The intensity of the measured autocorrelation function g_2 can be then fitted to $g_2 = 1 + 2(1 - j_d) j_d g_1 + j_d^2 g_1^2$, being j_d the ratio between the intensity of the inelastically scattered light and the total scattered intensity. In the measurements reported below for the comparison with DDM experiments in sections *Classic nematic E7* and *N-N_F phase transition*, g_1 is taken as a single exponential function.

DDM and c-DDM

The orientational fluctuations are easily observed by polarised optical microscopy as the flickering characteristic of the nematic phase. This flickering can be measured to extract information about the fluctuating modes. In the DDM, using a standard microscope with incoherent illumination, a sequence of near-field images is taken with a CCD or CMOS camera. From the intensity of the image $I(\mathbf{r}_{2D}, t)$ at pixel position $\mathbf{r}_{2D}$ and time t, the image structure function can be calculated [24]

$$F(\mathbf{q}_{2D}, \Delta t) = \left\langle \left| \Delta \tilde{I}(\mathbf{q}_{2D}, \Delta t) \right|^2 \right\rangle$$
$$= 2 \left\langle \left| \tilde{I}(\mathbf{q}_{2D}, 0) \right|^2 \right\rangle \left(1 - g_{incoh}^{(2)}(\mathbf{q}_{2D}, \Delta t)\right) \qquad (29)$$

$$g_{incoh}^{(2)}(\mathbf{q}_{2D}, \Delta t) = \frac{\left\langle \left| \tilde{I}^*(\mathbf{q}_{2D}, 0) \tilde{I}(\mathbf{q}_{2D}, \Delta t) \right| \right\rangle}{\left\langle \left| \tilde{I}(\mathbf{q}_{2D,}) \right|^2 \right\rangle} \qquad (30)$$

where $\Delta \tilde{I}(\mathbf{q}_{2D}, \Delta t)$ is the difference between the two-dimensional Fourier transforms of the two images taken at a time difference Δt, and $\tilde{I}(\mathbf{q}_{2D}, \Delta t) = \frac{1}{2\pi} \iint^I (\mathbf{r}_{2D}, \Delta t)^{-i\mathbf{q}_{2D} \cdot \mathbf{r}_{2D}} d\mathbf{r}_{2D}$ with $\mathbf{q}_{2D} \equiv (q_x, q_y)$. The average $\langle \dots \rangle$ is taken over many statistically independent realisations of the
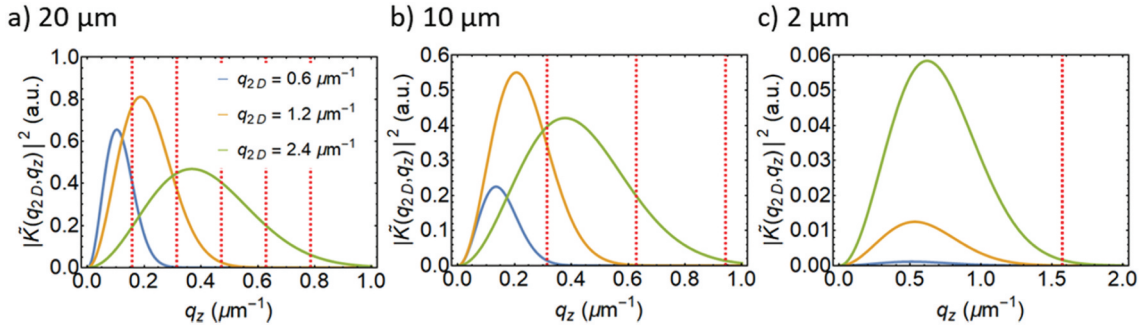

Figure 2. (Colour Online) Dynamic light scattering geometries to gain experimental access to (a) pure bend ($a = 35°$), (b) pure twist ($a = 2°$) and pure splay ($a = 35°$) modes.

Figure 3. (Colour Online) Weight functions for thicknesses (a) 20 μm, (b) 10 μm and (c) 2 μm. The discrete values of z-components of wavevectors corresponding to eigenmodes in confinement $\frac{N\pi}{d}$ are denoted for each thickness by vertical dashed red lines.

system, which in ergodic systems is the same as the average over time.

To model the measured image intensity, Giavazzi et al. [25] proposed to use the Nemoto-Streibl model of a microscope, for which the image on the camera in the weak scattering regime is written

$$I(\mathbf{r}_{2D}, t) = I_0 + \iiint d\mathbf{r}'_{2D} dz' K(\mathbf{r}_{2D} - \mathbf{r}'_{2D}, -z') \delta\varepsilon_{if}(\mathbf{r}'_{2D}, -z', t)$$

(31)

where $K(\mathbf{r}_{2D}, z)$ is the transfer function of the microscope that depends on the properties of the light source, condenser, objective and the orientation of the polariser and analyser. While I_0 is the directly transmitted light, $\delta\varepsilon_{if}(\mathbf{r}'_{2D}, -z', t)$ is the fluctuating part of a given component of the optical dielectric tensor chosen by the polariser and analyser.

In a DLS experiment, well-defined wave vectors and polarisations of incoming and scattered light define the scattering vector $\mathbf{q}$ and the geometrical factors S_β, which tell whether splay-bend or/and twist-bend mode contribute and, if both modes contribute, which is the more pronounced. In DDM experiments, the incoming light is spatially incoherent, i.e. there is a distribution of wave vectors $\mathbf{k}_i$ and $\mathbf{k}_f$ of incoming and scattered light respectively, and consequently, the scattered intensity $\tilde{I}(\mathbf{q}_{2D}, \Delta t)$ at a given 2D scattering vector $\mathbf{q}_{2D}$ is a weighted sum over all possible combinations of $\mathbf{k}_i$ and $\mathbf{k}_f$ that correspond to that given $\mathbf{q}_{2D}$. The 3D scattering vectors that contribute to the detected intensity are in principle all that satisfy the condition: $\mathbf{q} \equiv (\mathbf{q}_{2D}, q_z) = \mathbf{k}_f - \mathbf{k}_i$, which means that scattering processes with different q_z contribute to the scattered intensity at a given $\mathbf{q}_{2D}$. However, the strength of the contribution of a given q_z depends on the transfer function of the microscope. It has been shown that this leads to an expression for the image correlation function [25]

$$g_{incoh}^{(2)}(\mathbf{q}_{2D}, \Delta t) = A(\mathbf{q}_{2D}) \int dq_z |\tilde{K}(\mathbf{q}_{2D}, q_z)|^2$$

(32)

$$B(\mathbf{i}, \mathbf{k}_i \to \mathbf{f}, \mathbf{k}_f, t)$$

Here, the intermediate scattering function from Ref [25] is replaced with a more general dynamic structure function (Eq. 25), and $A(\mathbf{q}_{2D})$ is the normalization constant, $A(\mathbf{q}_{2D})^{-1} = \int^d q_z |\tilde{K}(\mathbf{q}_{2D}, q_z)|^2 B(\mathbf{i}, \mathbf{k}_i \to \mathbf{f}, \mathbf{k}_f, 0)$. In Ref [25], it has been shown that for a process with $B(\mathbf{i}, \mathbf{k}_i \to \mathbf{f}, \mathbf{k}_f, t) = Ae^{-Dq_z^2 - D_{xy}q^2}$, the image correlation function $g_{incoh}^{(2)}(\mathbf{q}_{2D}, \Delta t) \approx e^{-D_{xy}q^2_{2D}}$, which effectively means the dynamics at $q_z = 0$ is probed as a function of $\mathbf{q}_{2D}$.

The applicability of DDM for the characterisation of the dynamics of bulk nematic liquid crystals has been demonstrated in Ref [33]. However, in DDM experiments the liquid crystals are typically confined to layers with thicknesses from a few microns to a few tens of microns, which affects the measured $g_{incoh}^{(2)}(\mathbf{q}_{2D}, \Delta t)$ in two ways. The first, described in [25], causes broadening of the weight $|\tilde{K}(\mathbf{q}_{2D}, q_z)|^2$; the second described in the section *Effect of confinement* causes discrete eigenvalues of fluctuating eigenmodes. As a result, the image correlation function is a sum of a few eigenmodes with z-component of the eigenvector within the region where the weight $|\tilde{K}(\mathbf{q}_{2D}, q_z)|^2$ is significant (Figure 3).

Experimental details

Besides the weight in Eq. 32 the contribution of a given mode to the measured intensity depends also on its amplitude and geometrical factor as described by Eq. 27. In the following, we will focus on a nematic layer in a planar LC cell, with $\mathbf{n}_0$ oriented along the rubbing direction. In Figure 4, the dependence of the squares of the geometrical factors S_1 and S_2 are shown for two typical geometries. In the first, denoted by E10O
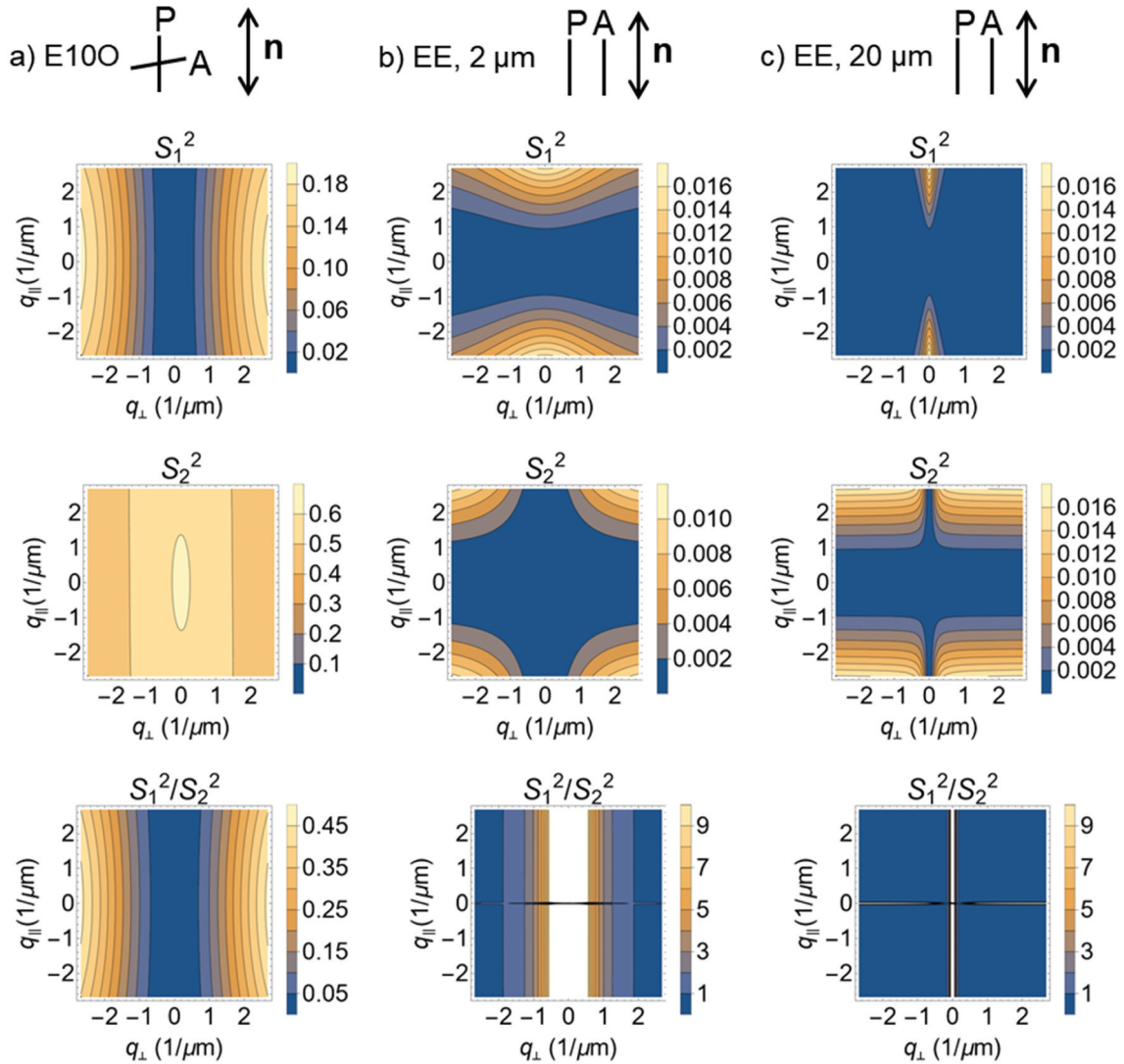
Figure 4. (Colour Online) Selection rules for the (a) E10O and (b–c) EE geometries showing that in the first case, the twist-bend mode dominates, while for the second geometry splay-bend mode is only dominant the region of small $q_\perp$. For EE geometry two cases are given: (b) a thin 2 µm thickness layer and (c) a thicker 20 µm one. P and a are the polarizer and analyser, respectively and **n** denotes the director.

(E for extraordinary and O for ordinary polarization), the polarizer is at an angle of 10 degrees with respect to $\mathbf{n}_0$ and the analyzer is perpendicular to $\mathbf{n}_0$. This geometry corresponds to the EO scattering geometry typical for DLS. The polarizer is uncrossed for 10 degrees, so that the detected signal with O polarization is mixed with directly transmitted O polarized light to achieve hetero-dyning [42]. Calculation of the geometrical factors S_β in this geometry allows to visualize the selection rules (Eq. 26), showing that in the case of E10O geometry the twist-bend mode dominates. In the second geometry, EE, both the polarizer and analyzer are parallel to $\mathbf{n}_0$. It is chosen to probe the splay-bend mode. However, it should be noted that the values of S_1 and S_2 in this geometry are comparable and much smaller than in E10O geometry. That is why the twist-bend mode is also present and the splay-bend is dominant only in the region with small $q_\perp$. The width of such a region depends on the thickness of the nematic layer, e.g. for a 20-micron thick the region is much narrower than for a 2-micron layer as shown in Figure 4. One should note here that the geometrical factors depicted in Figure 4 will directly determine the accessible modes via DDM only in those cases where elastic constants K_1 and K_2 are comparable. In cases in which elastic constants drastically change or differ, such as in the case of the transition to the ferroelectric nematic phase, the region of accessibility to splay-bend mode expands (Eq. 24) as will be discussed later.

In the experiments, the c-DDM setup extensively described in Ref [32] was used. It consists of an infinity-corrected microscope objective with a 20× magnification, a 20 mm focal length tube lens followed by a beamsplitter, and two identical cameras (Flir BFS-U3 -04S2CCS with 6.9 μm pixel size and 1/3 inch sensor). The precise alignment of the field of view of both cameras is achieved by aligning the cameras with an alignment ruler using translational and rotational mechanisms. Koehler illumination setup is used, consisting of a Thorlab's M565L3 mounted phosphor-converted LED with a nominal wavelength of 565 nm and a bandwidth of 100 nm. Cameras were triggered as described in reference [20] to acquire two different sets of images with varying times of acquisition. Camera exposure time was 21 μs, and we set the shortest time delay between two consecutive frames on cameras to 250 μs. To calculate the normalised image-cross-correlation function an open-source package cddm is used [44].

Systems

Classic nematic E7

In order to give a comprehensive overview of the performance of DDM in confined nematic LC, the standard liquid crystal mixture E7 (Merck) was filled in planar cells with thicknesses 23.5, 10, 8.3, 5.6 and 1.9 microns. The c-DDM was performed on all samples at room temperature (23°C) in geometries depicted in Figure 4. The measured autocorrelation functions $g_{incoh}^{(2)}(\mathbf{q}_{2D}, \Delta t)$ showed one relaxation, which was fitted by an exponential function $A_0 e^{-\Delta t/\tau} + y0$. In Figure 5, the 2D dispersion relation, i.e. the dependence of the relaxation rates $1/\tau$ on $\mathbf{q}_{2D}$, is shown.

E10O geometry. In this case, the relaxation rates along ($q_\parallel$), and perpendicular ($q_\perp$) to $\mathbf{n}_0$ are independent of the thickness. Confinement does not have an effect here because the accessible q_z are determined by the incoming $\mathbf{k}_i = (0, 0, n_e k_0)$ and outgoing $\mathbf{k}_f = \left(q_\perp, q_\parallel, \sqrt{(n_o k_0)^2 - q_\perp^2 - q_\parallel^2}\right)$. For $q_\perp, q_\parallel \ll k_0$ as characteristic of DDM, it follows $\mathbf{q} \approx \left(q_\perp, q_\parallel, \varepsilon_a k_0 - \left(q_\perp^2 + q_\parallel^2\right)/(2n_e k_0)\right)$, which means q_z is much larger than π/d, so the discretization of the eigenmodes can be neglected. Here, n_e and n_o are extraordinary and ordinary refractive index, respectively.

In this case for $q_\parallel = 0$, the twist-bend relaxation rate (Eq. 2), simplifies to

$$\frac{1}{\tau_2} = \frac{K_2}{\gamma_1}\left(q_{eo}^2 + \frac{n_e}{n_o} q_\perp^2\right). \qquad (33)$$

Here $q_{eo} = (n_e - n_o)k_0$ is determined by the optical anisotropy of the material. From the fit, the diffusivity $\frac{K_2}{\gamma_1} = (4.2 \pm 0.2) \cdot 10^{-11} \mathrm{m}^2/\mathrm{s}$ and $q_{eo} = (2.1 \pm 0.1)\mu\mathrm{m}^{-1}$ are obtained (Figure 5(f)). For comparison, in Figure 5(f), the relaxation rates as measured by DLS in the same geometry are shown. The DLS values are larger because the wavelength of the laser (532 nm) is smaller than that of the LED used in c-DDM (565 nm) which causes the offset at $q_\perp = 0$ to be larger larger. If the DLS relaxation rates are shifted for $\frac{K_2}{\gamma_1}(n_e - n_o)^2\left(\left(\frac{2\pi}{\lambda_{\mathrm{laser}}}\right)^2 - \left(\frac{2\pi}{\lambda_{\mathrm{LED}}}\right)^2\right)$, the values are very good agreement with those measured in the c-DDM.

Similarly, for $q_\perp = 0$, the twist-bend relaxation rate (Eq 2) can be rewritten

$$\frac{1}{\tau_2} = \frac{K_2}{\gamma_1} q_{eo}^2 \left(\frac{1 + a_2\left(\frac{q_\parallel}{q_{eo}}\right)^2 + a_4\left(\frac{q_\parallel}{q_{eo}}\right)^4}{1 + b_2\left(\frac{q_\parallel}{q_{eo}}\right)^2}\right). \qquad (34)$$

$$a_2 = 2\frac{n_e}{n_o} - 2 + \frac{K_3}{K_2} + \frac{\eta_c}{\eta_a},$$

$$a_4 = \left(\frac{n_e}{n_o} - 1 + \frac{K_3}{K_2}\right)\left(\frac{n_e}{n_o} - 1 + \frac{\eta_c}{\eta_a}\right),$$

$$b_2 = \frac{n_e}{n_o} - 1 + \frac{\eta_c}{\eta_a} - \frac{\alpha_2^2}{\gamma_1 \eta_a}$$

In principle, by taking the values for $\frac{K_2}{\gamma_1} q_{eo}^2$ and q_{eo} from the fit of the $q_\perp$- dependence (Equation 34. 34), there are only 3 parameters to the fit $q_\parallel$- dependence. However, for E7 these parameters are such that for the region of $\frac{q_\parallel}{q_{eo}}$ obtained in the experiment, they cannot be reliably determined.

In the EE geometry, there is a strong thickness dependence whose sources are multifold. Firstly, the confinement causes the eigenvalues to become discrete, which means that at $q_\parallel = 0$ and $q_\perp = 0$, for strong anchoring the pure splay mode with $q_{m,z} = \pi/d$ would be measured. The geometric factor S_1 is zero in this case, however, in Figure 5(e) it can be seen that the relaxation rates indeed increase with decreasing thickness. Secondly, the coupling to flow causes changes in the eigenmodes, so that they are no longer plane waves [39], and, consequently, the dispersion relation, i.e. the dependence of the relaxation rates on $\mathbf{q}$, can no longer be analytically expressed. It can only be calculated numerically when all the viscoelastic parameters are known. For 5CB, the numerical calculations have shown that the first eigenmode roughly corresponds to the slowest eigenmode, which for small $q_\parallel$ is that with
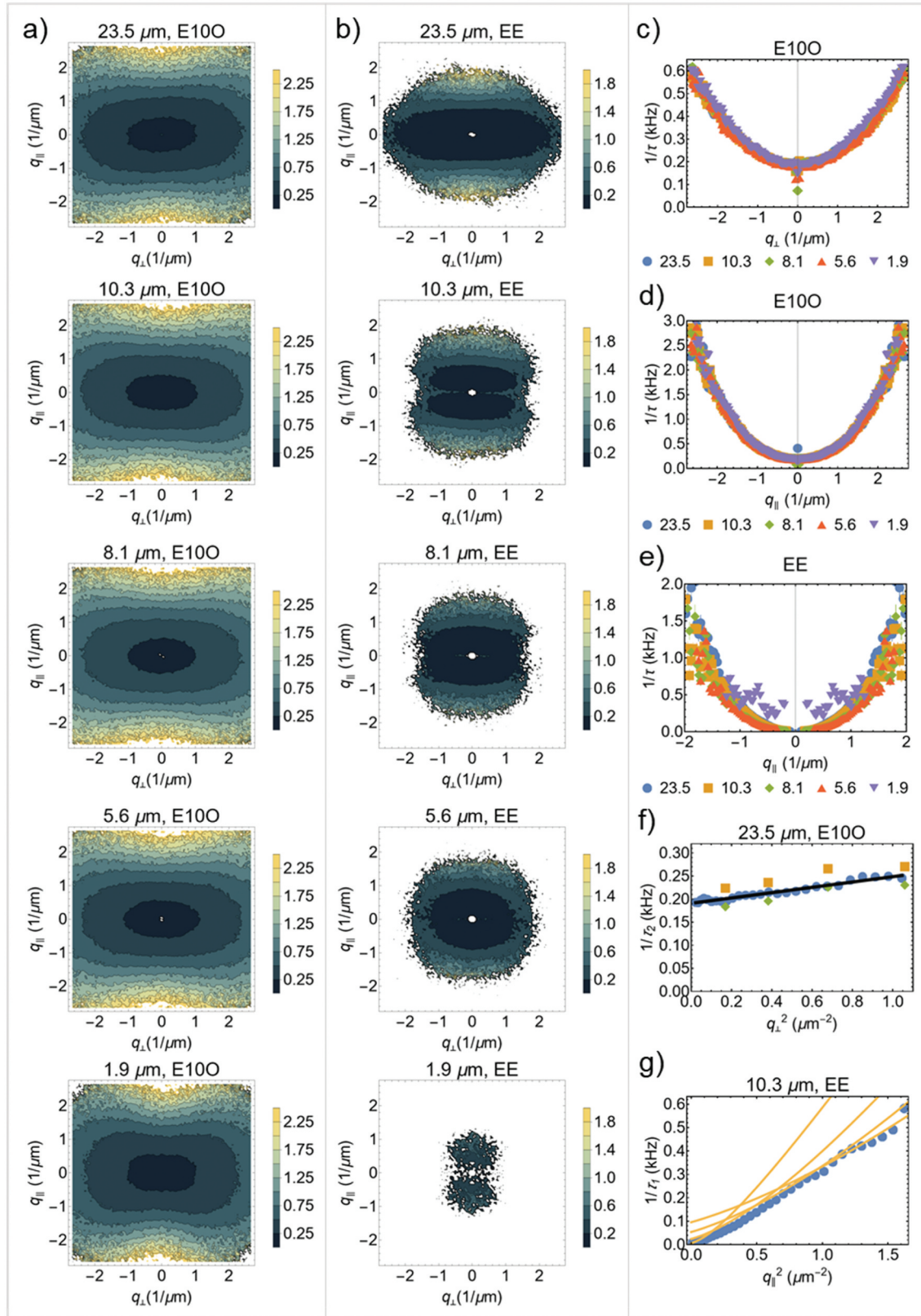
Figure 5. (Colour Online) 2D dispersion curves as measured by c-DDM for classic nematic liquid crystal E7 in planar cells with different thicknesses in (a) E10O and (b) EE geometries. (c) and (d) dispersion curves along c) $q_\perp$ and d) $q_\parallel$ axes for E10O geometry and (e) along $q_\parallel$ axis for EE geometry. (f) the twist relaxation rate (E10O) as a function $q_\perp^2$ (blue circles) with linear fit (black line) and comparison with DLS (orange squares) and shifted DLS (green diamonds). (g) the splay bend relaxation rate (EE) as a function $q_\parallel^2$ (blue circles) and the rates for the first four modes calculated for bulk (orange lines).

$q_{m,z} = \pi/d$, but with increasing $q_\parallel$ the mode with $q_{m,z} = 3\pi/d$ becomes slower, for even higher $q_\parallel$ the one with $q_{m,z} = 5\pi/d$ etc. [39]. Similarly, the second mode corresponds to a combination of even modes with $q_{m,z} = \frac{2N\pi}{d}$, $(N = 1, 2..)$. In Figure 5(g), the dispersion of a few lowest modes as calculated from analytical expression for bulk (Equation 2) are shown together with measured dispersion. Thirdly, the contribution of the modes to the scattering intensity decreases with decreasing thickness which is a consequence of $q_{m,z}$ falling out of the region where the weight function is significant (Figure 3).

To sum up, in DDM experiments the E10O geometry allows us to measure the twist bend mode and to determine the twist diffusivity. On the other hand, in the EE geometry for $q_\perp = 0$, the splay bend mode is observed; however, it is strongly affected by the confinement, which needs to be accounted for in the further analysis. The elongated shape of 2D dispersion curves in both geometries reflects two facts: that the K_3 is larger than K_2 and K_1 and, additionally, that bend viscosity is reduced significantly more by the backflow. Thus it is expected that any changes in ratios of elastic constants and/ or viscosity coefficients will change the shape of 2D dispersion curves.

N-N$_{TB}$ phase transition

DLS studies of nematic phases above the N$_{TB}$ transition revealed strong softening of bend fluctuations, which was attributed to the softening of bend elastic constant [3,9,45], and thus constitute an excellent system to
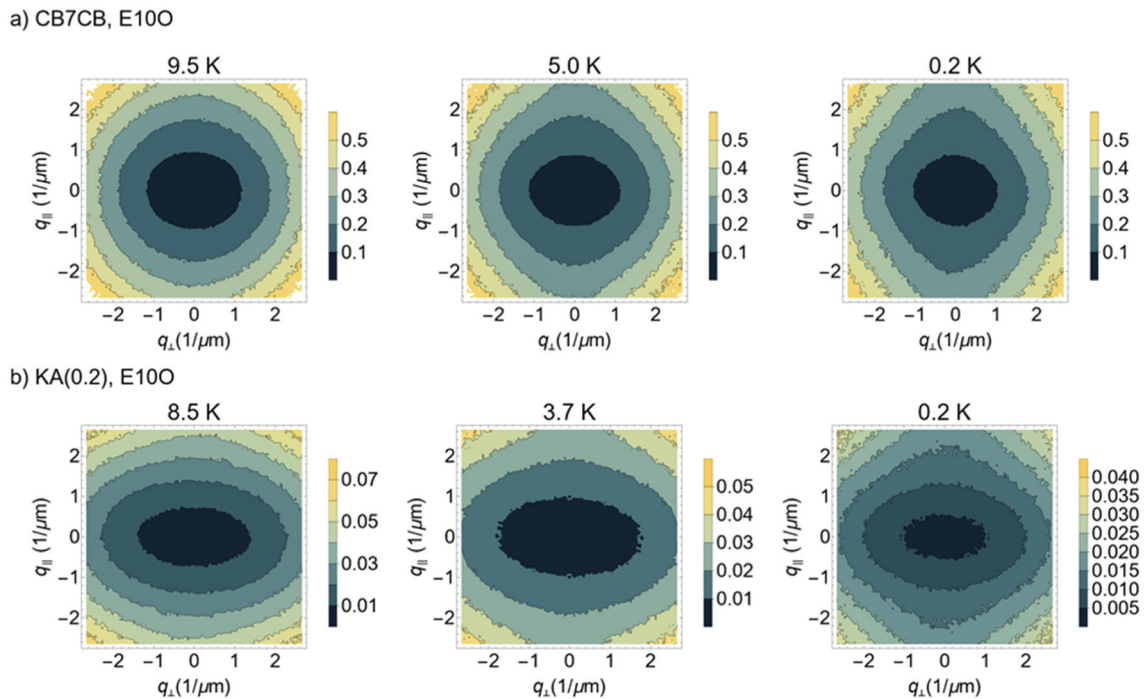

Figure 6. (Colour Online) 2D dispersion curves in E10O geometry for (a) CB7CB and (b) KA(0.2) for different $\Delta T = T - T_{N-N_{TB}}$.
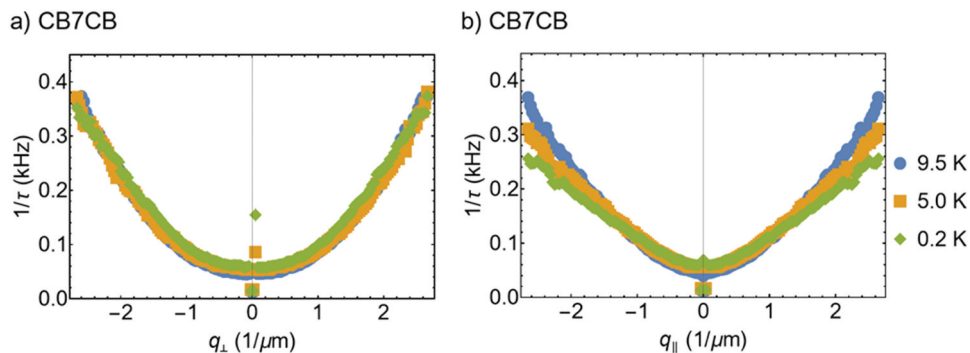

Figure 7. (Colour Online) Dispersion curves along (a) $q_\perp$ and (b) $q_\parallel$ axes for CB7CB in the E10O geometry.

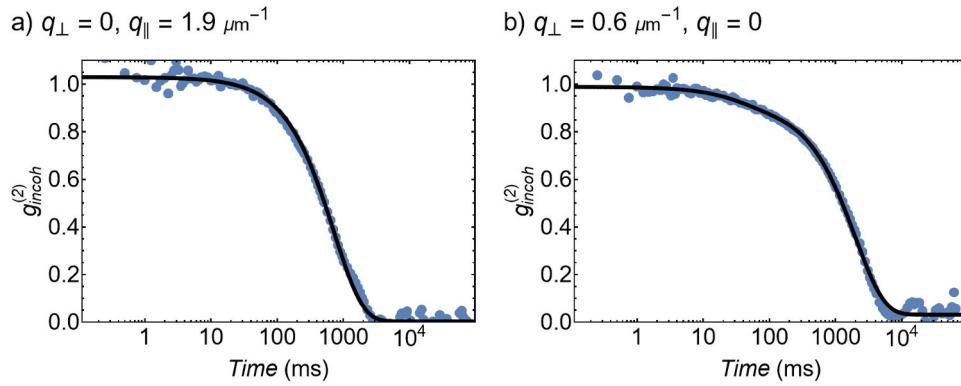a) $q_\perp = 0$, $q_\parallel = 1.9\ \mu m^{-1}$ b) $q_\perp = 0.6\ \mu m^{-1}$, $q_\parallel = 0$

Figure 8. (Colour Online) Examples of the correlation function for KA(0.2) at $T - T_{N-N_{TB}} = 0.2K$ in EE geometry (a) in the region with one mode and b) two modes. Lines are the fits to a) single and (b) double exponential functions.

evaluate the potentialities of the cDDM technique for the investigation of pretransitional behaviour in nematic phases. For this purpose, the liquid crystalline materials CB7CB (Merck) and the mixture KA(0.2) [3] filled in planar cells with thicknesses 20 μm and 25 μm, respectively, were studied by cDDM in the same scattering geometries as E7. In Figures 6–8, the 2D dispersion curves are shown, and, in both geometries and for both materials, there is a clear difference in comparison to E7 (Figure 5).

E10O geometry. Away from the N to N_{TB} phase transition, the shape of the 2D dispersion curve is similar to that measured in E7. The main difference is that it is less

anisotropic, which can be attributed to the small anisotropy of the elastic constants in the case of the dimers, i.e. the smaller value of K_3 when compared with E7 results in slower fluctuation rates in the $q_\parallel$ direction. When approaching the phase transition, the shape of the 2D dispersion changes – it becomes more diamond-like and, while in $q_\perp$ direction still shows q^2 dependence, in $q_\parallel$ direction it clearly deviates from it (Figure 7(a,b)). This diamond shape observed in both materials seems to be a characteristic pretransitional feature mirroring a specific combination of elastic and viscous coefficients. The latter to our best knowledge have not been measured in this system. From DLS experiments, in principle, viscosities of pure twist, bend and splay
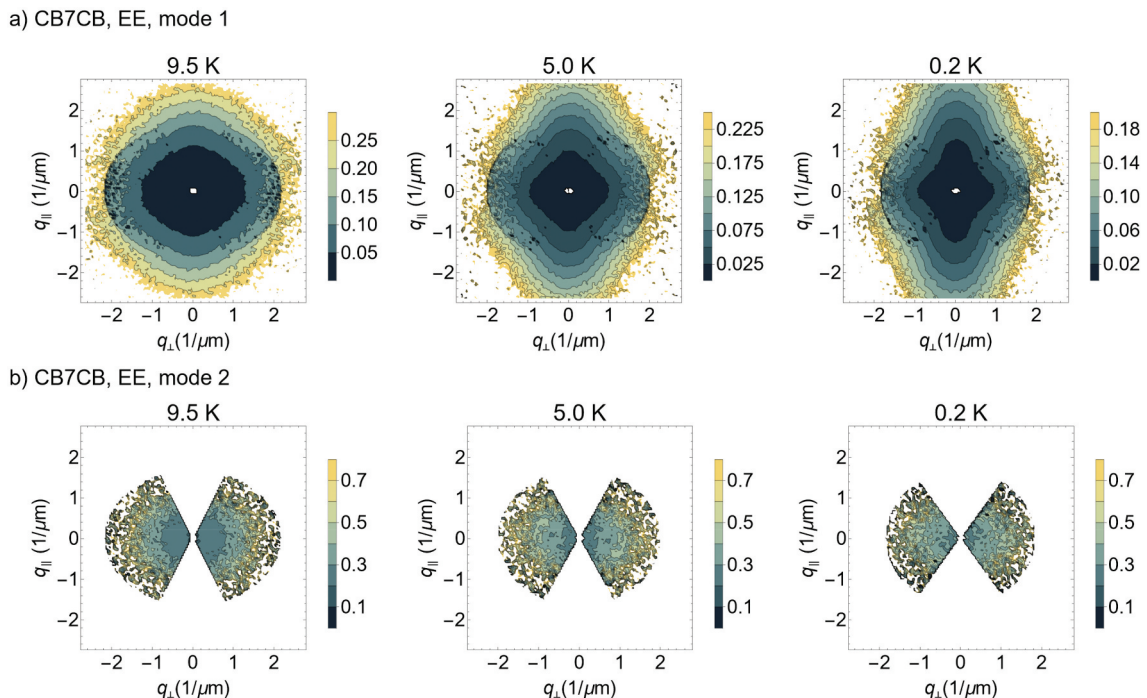
a) CB7CB, EE, mode 1

b) CB7CB, EE, mode 2

Figure 9. (Colour Online) 2D dispersion curves in EE geometry for CB7CB for a) mode 1 and b) mode 2 for different $\Delta T = T - T_{N-N_{TB}}$.

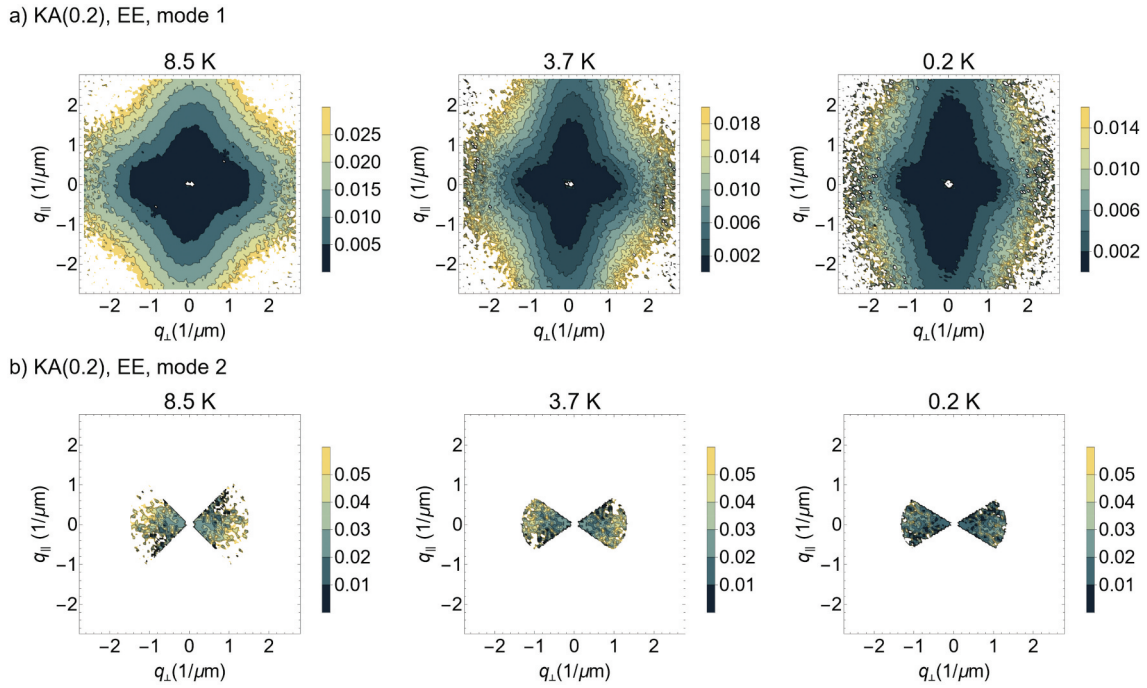a) KA(0.2), EE, mode 1

b) KA(0.2), EE, mode 2

Figure 10. (Colour Online) 2D dispersion curves in EE geometry for KA(0.2) for (a) mode 1 and (b) mode 2 for different $\Delta T = T - T_{N-N_{TB}}$.

mode can be measured, but this is not sufficient to determine all 5 independent Leslie viscosities.

EE Geometry. Here, the shape of the 2D dispersion curve strongly deviates from that in E7 (see Figures 9 and 10), even at temperatures 10 degrees above the N-N_{TB} transition, showing slow relaxation rates in the $q_\parallel$ direction. This is mainly a consequence of the small K_3 value. Additionally, at small $q_\parallel$, where scattering the amplitudes of the splay-bend and twist-bend modes are very small, another faster relaxation is observed, which was more pronounced in the CB7CB case. Thus, the correlation functions in that region were fitted by two exponential decay (Figure 8). The 2D dispersion

curves for both modes are shown in Figures 9 and 10, where the faster relaxation is denoted by mode 2.

To elucidate the nature of this faster relaxation, we checked other scattering geometries and found that it is present also in the OO geometry (where both polariser and analyser are perpendicular to **n**), in which the splay-bend and twist-bend geometric factors S_1 and S_2 are 0 and no signal is expected. However, in the OO geometry clear signal is detected with the measured 2D dispersion curve being symmetric, i.e. it depends on the value of $\mathbf{q}_{2D}$ but not on its direction (Figure 11(a)). The values match those measured for mode 2 in EE geometry (Figure 11(b)). To obtain the relaxation rate at $\mathbf{q}_{2D} = 0$, the dispersion curves of mode 2 in $q_\perp$ direction
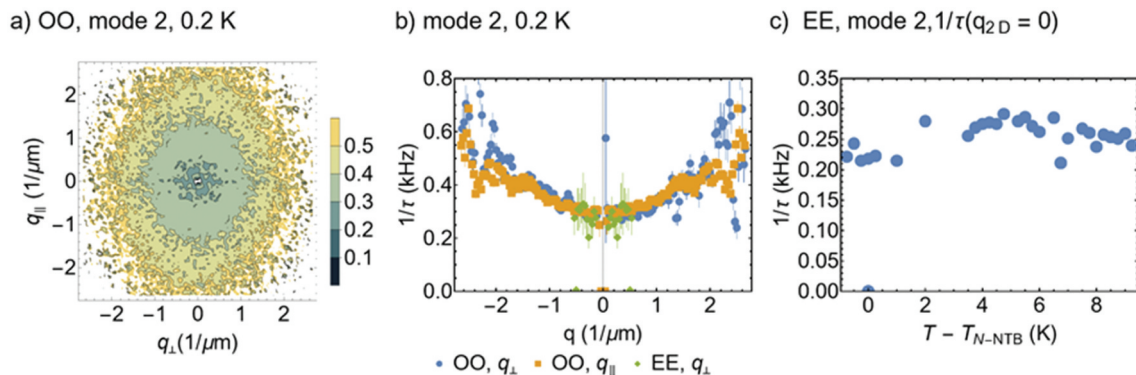
a) OO, mode 2, 0.2 K   b) mode 2, 0.2 K   c) EE, mode 2, $1/\tau(q_{2D} = 0)$

Figure 11. (Colour Online) (a) 2D dispersion curve in OO geometry for CB7CB. (b) comparison of the dispersion curves along $q_\parallel$ and $q_\perp$ axes in OO geometry and EE geometry. (c) Temperature dependence of the offset of the dispersion curve of mode 2 at $\mathbf{q}_{2D} = 0$.

were fitted with a quadratic function. In the measured temperature range (0–10 K above the N-N$_{TB}$ phase transition) it doesn't exhibit any significant temperature dependence ((Figure 11(c)) and, additionally, it is also observed below the phase transition.

In the OO and partially in the EE geometries, the diagonal elements of the optical dielectric tensors (Eq. 23) are probed. These components depend on the scalar order parameter S and, if present, on the biaxiality B of the system. The biaxiality fluctuations could originate from the bend flexoelectric coupling as discussed in Section *Coupling to other (order) parameters*. The polarization in such a case would be replaced by shape polarity (as also discussed by Longa et al. [10]), and the relaxation rate at $\mathbf{q}_{2D} = 0$ would be equal to a/η_P, where a is the Landau parameter (Eq. 22). If the emerging polar order is the driving mechanism for the N-N$_{TB}$ phase transition, then $a = a_0(T - T^*_{N-NTB})$, which would result in the slowing down of the mode when approaching the phase transition. Additionally, for molecules having a nonzero component of the dipole moment perpendicular to the long axis, this mode would be also seen in dielectric spectra as a collective mode at the frequency around 0.2–0.3 kHz. This has not been observed in CB7CB, however, in this frequency regime in dielectric spectroscopy there are other contributions to the spectra arising from conductivity and electrode polarisation effects. Another possibility is that the origin of mode 2 is connected to the fluctuation of the scalar order parameter. This question remains open to further investigation.

N-N$_F$ phase transition. DLS studies of the nematic phase above the N-N$_F$ transition revealed strong pretransitional softening of splay fluctuations, which was attributed to the softening of the splay elastic constant [20,21]. Here we compare DLS results with the accessible pretransitional behaviour via cDDM measurements. For that, we investigated RM734 confined in 20 μm cell (Instec) with antiparallel rubbing.

In Figure 12(a) the 2D dispersion curves measured EO10 geometry are shown. In this geometry for K_1 larger than K_2, the twist bend mode dominates in almost the entire range of $\mathbf{q}_{2D}$s (Figure 4(a)). However, for RM734, in the region of larger $q_\perp$, it can be clearly seen how the dispersion curve gets broader with decreasing temperature reflecting a significant slowing down of the relaxation rates in that region of $\mathbf{q}$s. If one takes into consideration a decreasing splay elastic constant, then it follows that the ratio between the scattering amplitudes $\frac{K_2}{K_1}\left(\frac{S_1}{S_2}\right)^2$ in this region is increasing and, consequently, at this larger $\mathbf{q}$s mostly the splay-bend mode contributes, while at small $q_\perp$ the twist-bend still dominates. That is the reason why in Figure 12(b) for $\Delta T = 1.3K$ and $0.3K$ there is an increase of relaxation rate when $q_\perp$ approaches zero. The splay diffusivity was calculated by averaging $\frac{\frac{1}{\tau}}{\left(q_{eo}^2 + \frac{n_e}{n_o}q_\perp^2\right)}$ in the region $q_\parallel = 0, q_\perp > 2\mu m^{-1}$, while the twist was obtained by $\frac{\frac{1}{\tau 0}}{\left(q_{eo}^2\right)}$, where $\frac{1}{\tau 0}$ is the value at $q_\parallel = 0, q_\perp = 0$ and was determined by fitting the middle part (from 0.5 μm^{-1} to 0.5 μm^{-1}) of $q_\parallel$-dependence
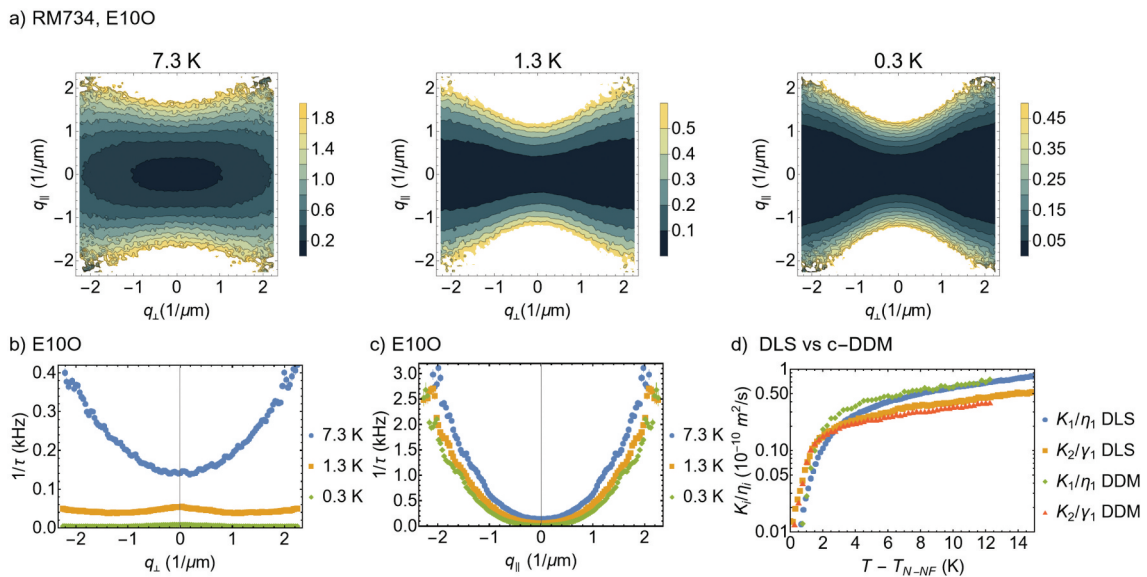

a) RM734, E10O

Figure 12. (a) 2D dispersion curves at E10O geometry for RM734 at 3 selected temperatures above phase transition. The values above graphs are $\Delta T = T - T_{NN_F}$. (b) and (c) show the dispersions along $q_\perp$ and $q_\parallel$ axes. (d) comparison of the splay and the twist diffusivities measured by c-DDM and DLS.

(Figure 12(c)) by a quadratic function. In Figure 12(d) the temperature dependence of so obtained values is compared to those measured in the DLS experiments. The agreement is considerably good showing that at $q_\perp > 2\mu m^{-1}$ indeed splay-bend mode dominates.

Conclusions and outlook

The presented examples demonstrate the usability of DDM techniques for the investigation of nematic liquid crystalline systems. While its principle is similar to DLS, the methods are complementary. DLS is more sensitive and it can access faster dynamics at higher values of q. The strength of DDM is that it is a microscopy technique, which allows imaging of the part of the sample that is measured, which is particularly important when there are defects or impurities present which affect the system's dynamics. A huge advantage is also that in a single measurement correlation functions at many $\mathbf{q}$ are measured and the shape of the 2D dispersion curve gives information about the distinctive properties of the system and its symmetry. For example, in the case of the N_F phase, it has been shown that one can clearly distinguish the π-twist domains with different chirality [37]. The DLS measurements at small qs are often challenging because of the static scattering, and this is not an issue for the DDM. Our study of the nematic phase of dimeric materials also pointed out that modes corresponding to fluctuation of scalar order parameter or biaxiality (when sufficiently strong) can be detected by the DDM.

Acknowledgments

Disclosure statement

Funding

ORCID

Nerea Sebastián 🆔 http://orcid.org/0000-0002-9156-1895
Alenka Mertelj 🆔 http://orcid.org/0000-0002-2766-9121

References

[1] Dozov I. On the spontaneous symmetry breaking in the mesophases of achiral banana-shaped molecules. Europhys Lett. 2001;56(2):247. doi: 10.1209/epl/i2001-00513-x

[2] Cestari M, Diez-Berart S, Dunmur DA, et al. Phase behavior and properties of the liquid-crystal dimer 1″,7″-bis (4-cyanobiphenyl-4′-yl) heptane: a twist-bend nematic liquid crystal. Phys ReRv E [Internet]. 2011 [cited 2011 Oct 18] 18;84(3):031704. Available from: http://link.aps.org/doi/10.1103/PhysRevE.84.031704.

[3] Adlem K, Čopič M, Luckhurst GR, et al. Chemically induced twist-bend nematic liquid crystals, liquid crystal dimers, and negative elastic constants. Phys Rev E [Internet]. 2013 [cited 2013 Oct 4]; 88:022503. Available from: http://link.aps.org/doi/10.1103/PhysRevE.88.022503.

[4] Borshch V, Kim Y-K, Xiang J, et al. Nematic twist-bend phase with nanoscale modulation of molecular orientation. Nat Commun [Internet]. 2013 [cited 2018 Nov 7];4:2635. doi: 10.1038/ncomms3635

[5] Chen D, Porada JH, Hooper JB, et al. Chiral heliconical ground state of nanoscale pitch in a nematic liquid crystal of achiral molecular dimers. PNAS [Internet]. 2013 [cited 2013 Nov 9]: 201314654. Available from: http://www.pnas.org/content/early/2013/09/04/1314654110

[6] Jákli A, Lavrentovich OD, Selinger JV. Physics of liquid crystals of bent-shaped molecules. Rev Mod Phys [Internet]. 2018 [cited 2018 Nov 26];90:045004. Available from: https://link.aps.org/doi/10.1103/RevModPhys.90.045004.

[7] Mandle RJ. A ten-year perspective on twist-bend nematic materials. Molecules [Internet]. 2022[cited 2023 Dec 9];27(9):2689. doi: 10.3390/molecules27092689.

[8] Shamid SM, Dhakal S, Selinger JV. Statistical mechanics of bend flexoelectricity and the twist-bend phase in bent-core liquid crystals. Phys Rev E [Internet]. 2013 cited 2018 Apr 13;87(5):052503. doi: 10.1103/PhysRevE.87.052503.

[9] Čopič M, Mertelj A. Q-tensor model of twist-bend and splay nematic phases. Phys Rev E [Internet]. cited 2020 Feb 26 20202;101:022704. Available from: https://link.aps.org/doi/10.1103/PhysRevE.101.022704.

[10] Longa L, Pająk G. Modulated nematic structures induced by chirality and steric polarization. Phys Rev E [Internet]. 2016 cited 2018 Oct 15;93(4):040701. doi: 10.1103/PhysRevE.93.040701.

[11] Longa L, Tomczyk W. Twist-bend nematic phase in the presence of molecular chirality. Liq Cryst [Internet]. 2018 cited 2023 Dec 9;45:2074–2085. doi: 10.1080/02678292.2018.1499148.

[12] Pająk G, Longa L, Chrzanowska A. Nematic twist–bend phase in an external field. PNAS [Internet]. 2018 cited

2019 Sep 24;115(44):E10303–E10312. doi: 10.1073/pnas.1721786115.

[13] Longa L, Tomczyk W. Twist–bend nematic phase from the Landau–de gennes perspective. J Phys Chem C [Internet]. 2020 cited 2021 Oct 4;124 (41):22761–22775. doi: 10.1021/acs.jpcc.0c05711.

[14] Longa L, Cieśla M, Karbowniczek P, et al. Conformational degrees of freedom and stability of splay-bend ordering in the limit of a very strong planar anchoring. Phys Rev E [Internet]. 2023 cited 2023 Dec 9;107(3):034707. Available from: https://link.aps.org/doi/10.1103/PhysRevE.107.034707 .

[15] Tomczyk W, Longa L. Role of molecular bend angle and biaxiality in the stabilization of the twist-bend nematic phase. Soft Matter [Internet]. 2020 cited 2023 Dec 9;16(18):4350–4357. doi: 10.1039/D0SM00078G.

[16] Sebastián N, Čopič M, Mertelj A. Ferroelectric nematic liquid-crystalline phases. Phys Rev E [Internet]. cited 2022 Aug 17 20222;106:021001. Available from: https://link.aps.org/doi/10.1103/PhysRevE.106.021001 .

[17] Mandle RJ, Cowling SJ, Goodby JW. Rational design of rod-like liquid crystals exhibiting two nematic phases. Chem: Eur J [Internet]. 2017 cited 2018 Feb 2;23 (58):14554–14562. doi: 10.1002/chem.201702742.

[18] Mandle RJ, Cowling SJ, Goodby JW. A nematic to nematic transformation exhibited by a rod-like liquid crystal. Phys Chem Chem Phys [Internet]. 2017 cited 2018 Jan 31; 19 (18):11429–11435. doi: 10.1039/C7CP00456G.

[19] Nishikawa H, Shiroshita K, Higuchi H, et al. A fluid liquid-crystal material with highly polar order. Adv Mater [Internet]. 2017 cited 2018 Dec 18;29 (43):1702354. doi: 10.1002/adma.201702354

[20] Mertelj A, Cmok L, Sebastián N, et al. Splay nematic phase. Phys Rev X [Internet]. 2018 cited 2018 Dec 5;8 (4):041025. Available from: https://link.aps.org/doi/10.1103/PhysRevX.8.041025.

[21] Sebastián N, Cmok L, Mandle RJ, et al. Ferroelectric-ferroelastic phase transition in a nematic liquid crystal. Phys Rev Lett [Internet]. 2020 cited 2020 Jan 22;124 (3):037801. Available from: https://link.aps.org/doi/10.1103/PhysRevLett.124.037801 .

[22] Mandle RJ, Sebastián N, Martinez-Perdiguero J, et al. On the molecular origins of the ferroelectric splay nematic phase. Nat Commun [Internet]. 2021 cited 2021 Aug 23;12(1):4962. doi: 10.1038/s41467-021-25231-0

[23] de GP, Prost J. The physics of liquid crystals. 2nd ed. Oxford: Clarendon Press; 1995.

[24] Cerbino R, Trappe V. Differential dynamic microscopy: probing wave vector dependent dynamics with a microscope. Phys Rev Lett [Internet]. 2008 cited 2011 Oct 20; 100(18):188102. doi: 10.1103/PhysRevLett.100.188102.

[25] Giavazzi F, Brogioli D, Trappe V, et al. Scattering information obtained by optical microscopy: differential dynamic microscopy and beyond. Phys Rev E [Internet]. 2009 cited 2011 Oct 20;80(3):031403. doi: 10.1103/PhysRevE.80.031403

[26] Giavazzi F, Haro-Pérez C, Cerbino R. Simultaneous characterization of rotational and translational diffusion of optically anisotropic particles by optical microscopy. J Phys Condens Matter [Internet]. cited 2016 May 26 201619;28:195201. Available from: http://stacks.iop.org/0953-8984/28/i=19/a=195201 .

[27] Reufer M, Martinez VA, Schurtenberger P, et al. Differential dynamic microscopy for anisotropic colloidal dynamics. Langmuir [Internet]. 2012;28 (10):4618–4624. doi: 10.1021/la204904a

[28] Pal A, Martinez VA, Ito TH, et al. Anisotropic dynamics and kinetic arrest of dense colloidal ellipsoids in the presence of an external field studied by differential dynamic microscopy. Sci Adv [Internet]. 2020 cited 2021 Feb 3;6(3):eaaw9733. doi: 10.1126/sciadv.aaw9733

[29] Wilson LG, Martinez VA, Schwarz-Linek J, et al. Differential dynamic microscopy of bacterial motility. Phys Rev Lett [Internet]. 2011 cited 2011 Oct 20;106 (1):018101. Available from: http://link.aps.org/doi/10.1103/PhysRevLett.106.018101.

[30] Ferri F, D'Angelo A, Lee M, et al. Kinetics of colloidal fractal aggregation by differential dynamic microscopy. Eur Phys J Spec Top [Internet]. 2011 cited 2012 Jul 17;199(1):139–148. Available from: http://www.springerlink.com/content/775u10u506253357/abstract/.

[31] Wang J, McGorty R. Measuring capillary wave dynamics using differential dynamic microscopy. Soft Matter [Internet]. 2019 cited 2021 Feb 3; 15 (37):7412–7419. doi: 10.1039/C9SM01508F.

[32] Arko M, Petelin A. Cross-differential dynamic microscopy. Soft Matter [Internet]. 2019 cited 2019 Apr 17; 15(13):2791–2797. doi: 10.1039/C9SM00121B.

[33] Giavazzi F, Crotti S, Speciale A, et al. Viscoelasticity of nematic liquid crystals at a glance. Soft Matter [Internet]. 2014 cited 2014 Jun 6;10(22):3938–3949. doi: 10.1039/C4SM00145A

[34] Mertelj A, Osterman N, Lisjak D, et al. Magneto-optic and converse magnetoelectric effects in a ferromagnetic liquid crystal. Soft Matter [Internet]. 2014 [cited 2014 Sep 23]; Available from: http://pubs.rsc.org/en/content/articlelanding/2014/sm/c4sm01625d.

[35] Gregorin Ž, Sebastián N, Osterman N, et al. Dynamics of domain formation in a ferromagnetic fluid. J Mol Liq [Internet] 2022 cited 2022 Nov 21;366:120308. Available from: https://www.sciencedirect.com/science/article/pii/S0167732222018475.

[36] Poy G. Hidden traces of chirality in the fluctuations of a fully unwound cholesteric. Soft Matter [Internet]. 2023 cited 2023 Nov 23; 19(6):1115–1130. doi: 10.1039/D2SM01646J.

[37] Sebastián N, Mandle RJ, Petelin A, et al. Electrooptics of mm-scale polar domains in the ferroelectric nematic phase. Liq Cryst [Internet]. 2021 cited 2022 Feb 2;48 (14):2055–2071. Available from: doi: 10.1080/02678292.2021.1955417

[38] Mertelj A, M Č. Dynamic light scattering as a probe of orientational dynamics in confined liquid crystals. Phys Rev E [Internet]. cited 2012 Jul 16 20002;61:1622–1628. Available from: http://link.aps.org/doi/10.1103/PhysRevE.61.1622.

[39] Čopič M, Vilfan M, Mertelj A. Flow and anchoring effects on nematic fluctuations in confined geometry. Liq Cryst [Internet]. 2013 cited 2014 Apr 4; 40 (12):1646–1654. doi: 10.1080/02678292.2013.819129.

[40] de la FM, Dunmur D. Dielectric Properties of Liquid Crystals. Handbook Of Liquid Crystals [Internet]. Wienheim, Germany: Wiley-VCH Verlag GmbH & Co. KGaA; 2014 [cited 2019 Sep 24]. p. 1–46. Available from: https://onlinelibrary.wiley.com/doi/abs/10.1002/9783527671403.hlc025.

[41] Parsouzi Z, Shamid SM, Borshch V, et al. Fluctuation modes of a twist-bend nematic liquid crystal. Phys Rev X [Internet]. 2016 cited 2018 Mar 21;6(2):021041. doi: 10.1103/PhysRevX.6.021041

[42] Berne BJ, Pecora R. Dynamic light scattering: with applications to chemistry, biology, and physics. Mineola, New York: Courier Dover Publications; 2000.

[43] Gisler T, Rüger H, Egelhaaf SU, et al. Mode-selective dynamic light scattering: theory versus experimental realization. Appl Opt [Internet]. 1995 cited 2011 Jan 20;34(18):3546–3553. doi: 10.1364/AO.34.003546

[44] Petelin A. Cross-differential dynamic microscopy v. 0.2. [cited 2023 Dec 9]; Available from: https://zenodo.org/records/3800382.

[45] Babakhanova G, Parsouzi Z, Paladugu S, et al. Elastic and viscous properties of the nematic dimer CB7CB. Phys Rev E [Internet] 2017 [cited 2018 May 17];96:062704. doi: 10.1103/PhysRevE.96.062704